

Ground motion prediction maps using seismic microzonation data and machine learning

Federico Mori¹, Amerigo Mendicelli¹, Gaetano Falcone¹, Gianluca Acunzo¹, Rose Line Spacagna¹, Giuseppe Naso², Massimiliano Moscatelli¹

¹ CNR-IGAG, Consiglio Nazionale delle Ricerche, Istituto di Geologia Ambientale e Geoingegneria, Area della Ricerca di Roma 1, Via Salaria km 29.300, 00015 Monterotondo (Roma), Italy

² Presidenza del Consiglio dei Ministri, Dipartimento della Protezione Civile (DPC), via Vitorchiano 2, 00189 Roma, Italy

Correspondence to: Federico Mori (federico.mori@igag.cnr.it)

Abstract. Past seismic events worldwide demonstrated that damage and death toll depend on both the strong ground motion (i.e., source effects) and the local site effects. The variability of earthquake ground motion distribution is caused by local stratigraphic and/or topographic setting and buried morphologies, that can give rise to amplification and resonances with respect to the ground motion expected at the reference site. Therefore, local site conditions can affect an area with damage related to the full collapse or loss in functionality of facilities, roads, pipelines, and other lifelines. To this concern, the *near real time* prediction of ground motion variation over large areas is a crucial issue to support the rescue and operational interventions. A machine learning approach was adopted to produce ground motion prediction maps considering both stratigraphic and morphological conditions. A set of about 16,000 accelometric data and about 46,000 geological and geophysical data were retrieved from Italian and European databases. The intensity measures of interest were estimated based on 9 input proxies. The adopted machine learning regression model (i.e., Gaussian Process Regression) allows to improve both the precision and the accuracy in the estimation of the intensity measures with respect to the available *near real time* predictions methods (i.e., Ground Motion Prediction Equation and shaking maps). In addition, maps with a 50 m x 50 m resolution were generated providing a ground motion variability in agreement with the results of advanced numerical simulations based on detailed sub-soil models.

1 Introduction

Spatial distributions of ground motion induced by seismic events should be properly estimated to support risk mitigation policies over large areas. Moreover, seismic risk analysis, extended to spatially distributed anthropic systems, presents new challenges in characterising the seismic risk input, regarding the spatial correlation of the ground motion values. The ShakeMaps (Wald et al., 2021), provided by the US Geological Survey, is used globally for post-earthquake emergency management and response, engineering analyses, financial instruments, and other decision-making activities. Moreover, in Italy post-event ShakeMaps are delivered by the National Institute of Geophysics and Volcanology (Michellini et al., 2019;

ShakeMap, 2021). Such ShakeMaps are based on Ground Motion Prediction Equation (GMPE; Bindi et al., 2011, among the others) and data recorded from accelerometric stations when available.

Recently, artificial intelligence-based procedures were proposed to produce *near real time* ground motion in terms of acceleration time histories (Jozinović et al., 2021, Tamhidi et al., 2021) and Intensity Measure (briefly, IM; Kubo et al., 2020, among the others). In general, ground motion maps were generated using earthquake source parameters (location, magnitude, and the finite fault if available), IM (Peak Ground Acceleration, Peak Ground Velocity, and Spectral acceleration, briefly named PGA, PGV, and Sa, respectively) at the recording accelerometric stations and the mean shear wave velocity in the upper 30 m, V_{S30} , as a proxy to account for site lithostratigraphic amplifications. Having shaking maps only when the first location and magnitude estimation are available, Jozinović et al. (2021) propose to use waveforms to predict the ground motion intensity by means of a Machine Learning (briefly, ML) approach (i.e., it utilizes only a training set of earthquake waveforms recorded at a pre-configured network of recording stations). Moreover, ML has been adopted to produce seismic amplification factors maps, as in the Japan case study proposed by Kim et al. (2020), rather than to provide ground motion maps. Finally, Zhou et al. (2020) propose a seismic topographic effect prediction model.

Overall, the above-mentioned works have pointed out what follows:

- hypocentral depth (H), epicentral distance (R), and magnitude (M) are widely used to estimate ground motion over large areas considering the source effect; moreover, H, R, and M are provided few minutes after an earthquake;
- V_{S30} , the fundamental frequency of the deposit (f_0), and the depth to the engineering bedrock (H_{800}) are the key-parameters which well gauge the effect of local sub-soil conditions on the seismic wave propagation (i.e., lithostratigraphic effect);
- elevation (h), topographic gradients (h_x and h_y , where x and y are two orthogonal directions), and second-order topographic gradients (h_{xx} and h_{yy}) are proxies which allow to describe the morphological effects on the seismic amplification phenomena.

In this view, this work focuses on the improvement of ground motion prediction over large areas by using ML technique. The main task of this work is to suggest a procedure including all the main key-parameters together (i.e., H, R, M, V_{S30} , h, h_x , h_y , h_{xx} , h_{yy}).

Damage pattern induced by seismic events is related to both geological/geomorphological conditions and vulnerability of structures and infrastructures (Brando et al., 2020; Fayjaloun et al., 2021; Mori et al., 2020b, 2019). The ground motion prediction (i.e., seismic site response) is generally evaluated by means of numerical simulations which are time consuming and require well detailed models capable of properly represents sub-soil and topographic conditions (see for example, Bouckovalas and Papadimitriou, 2005; Falcone et al., 2020a, 2020b, 2018; Gatmiri and Arson, 2008; Gazetas, 1982; Luo et al., 2020; Moscatelli et al., 2020b; Pagliaroli et al., 2014; Pitilakis et al., 1999; Régnier et al., 2016, 2018).

Hence, ML approach was adopted to:

- i) implement H, R, and M parameters available few minutes after a seismic event;
- ii) include both lithostratigraphic (V_{S30}) and morphological effects (h, h_x , h_y , h_{xx} , h_{yy});
- iii) capture the spatial correlation at short distances (hundreds of meters) due to local site effects, which is essential for reliable hazard assessments.

The main results of these elaborations are ground motion prediction maps (i.e., PGA, PGV, Sa) with the resolution of 50 m x 50 m, which can reproduce the variability captured by advanced numerical modelling. Seismological data (i.e., H, R, M, PGA, PGV, and Sa) retrieved from European and Italian networks (Luzi et al., 2016, 2019, 2020), geological, geophysical, and geotechnical data from seismic microzonation (hereafter SM) studies (DPC, 2021), and morphological data (ALOS, 2021) are presented in § 2. The ML approach is discussed in § 3. In detail, the § 3.1 is focused on the adopted ML approach in term of training and validation phase. Performances, presented in terms of Root Mean Square Error (RMSE) and residuals (i.e., difference between the base-10 logarithms of observed and predicted values of PGA, PGV, and Sa), are compared to the results proposed by other studies (Jozinović et al., 2021; Michelini et al., 2019, Bindi et al., 2011). For the seismic sequence that hit Central Italy in 2016-2017, ML results and maps are shown in § 3.2 and § 4, respectively. Referring to the seismic event occurred in Central Italy on October 30, 2016, a test is proposed in § 3.2 in terms of residuals of the ground motion IMs (i.e., PGA, PGV, and Sa). Ground motion prediction maps for the Central Italy event occurred on August 24, 2016, (i.e., the first destructive event of the Central Italy seismic sequence for which a great amount of studies have been published) are shown in § 4 to enlighten the capability of the proposed ML approach to gauge the ground motion variability at the urban scale. Moreover, with reference to § 4.1, the ground motion profiles, based on the proposed ML approach, are compared with results obtained by means of two completely different methodologies: 2D numerical modelling of seismic site response (Gaudiosi et al., 2021; Giallini et al., 2020; Grelle et al., 2020) and with the mean values predicted by the Italian ShakeMaps (ShakeMap, 2021).

Finally, evaluation of the spatial correlation structure was studied to provide the relation between local site effects and spatial resolution of ground motion maps; results of such analysis were not reported in the main text since it is out of the scope but preliminary results in terms of sill and range are reported in the Appendix referring to the seismic event occurred on October 30, 2016 (i.e., the strongest of the Central Italy seismic sequence).

In a nutshell, the novelty of this work is the use of the ML approach based on the analysis of a huge database of geological, geophysical, and geotechnical data, built with SM studies for the entire Italian territory. The quality and quantity of this database allow a robust application of ML including the prediction of local site effects (i.e., lithostratigraphic and morphological) on the seismic ground motion.

2 Input and output data for machine learning training and validation

The input and output data for the training of ML approach, were classified into three categories: seismological, geophysical, and morphological data. The ML approach was based on 15'779 seismological data regarding the log10 geometric mean of the horizontal component (geoH) for each IM (i.e., PGA, PGV, and Sa at 0.3 s, 1.0 s, and 3.0 s). Each value recorded by the accelerometric station, named output data in Table 1 (i.e., data to be reproduced by means of ML), represents an observed datum. In addition, Table 1 lists the used 9 predictors, named input data. Fig. 1 shows the location of the selected accelerometric stations. Figs. 2 and 3 show the input and output data, respectively, adopted for the training phase of the selected ML approach

and presented in this section. Furthermore, some data distributions seem to be imbalanced (e.g., magnitude, M , and elevation, h , Fig. 2). An imbalanced training input dataset is characterised by an unequal distribution of values. For instance, focusing on Fig. 2 and M distribution, it results that the first and third quartile are 4.1 and 5.1, respectively. Moreover, focusing on elevation distribution, it results that the first and third quartile are 136 m and 761 m, respectively. Consequently, when the ML algorithm learns the imbalanced data (see for example, Kubo et al., 2020) the learning focus is mainly on the fit of ground motions with magnitude lower than 6 or on the fit of site characterised by elevation lower than 1,200 m. The imbalance of the selected training input dataset seems to be caused by a sampling bias since no high magnitude ground motions were registered by the available accelerometric stations and since few accelerometric stations have been installed at high elevation where the exposition at seismic event is very low. Hence, it seems a hard task to improve the training dataset. In addition, distributions of topographic gradients and V_{S30} are characterised by few data with respect to steep slopes and high V_{S30} values. Anyway, how to handle the imbalanced dataset in the regression problem was out of the scope of this work. Consequently, referring to a range of an input datum, it is expected that the lower the amount of training data the higher the uncertainty. To this end, referring to the output data, maps of standard deviation are reported in § 4.1.

Table 1. Input and output data for ML training and validation.

Type of data	Category	Control Factors	Database	Ref.
INPUT	Seismological	H	hypocentral depth	Luzi et al., 2016 and 2020
		M	moment magnitude	Seismological DB
		R	epicentral distance	
	Geophysical	V_{S30}	the time-averaged shear-wave velocity to 30 m depth	Seismological DB or V_{S30} map
				Luzi et al., 2016 and 2020 DPC, 2021 Mori et al., 2020b
	Morphological	h	elevation	ALOS, 2021
		h_x	first order partial derivative dx (E-W slope)	ALOS World 3D-30m DEM
		h_y	first order partial derivative dy (N-S slope)	
		h_{xx}	second order partial derivative dyy	
		h_{yy}	second order partial derivative dxx	

OUTPUT	Seismological	PGA	Peak Ground Acceleration	Seismological DB	Luzi et al., 2016 and 2020
		PGV	Peak Ground Velocity		
		Sa _{0.3}	Spectral acceleration at 0.3 s		
		Sa _{1.0}	Spectral acceleration at 1 s		
		Sa _{3.0}	Spectral acceleration at 3 s		

Seismological parameters

Seismological parameters are retrieved from Italian and European databases. Regarding 1,435 recording accelerometric stations, PGA, PGV, spectral accelerations (i.e., Sa at 0.3 s, 1 s, and 3 s), H, R, and M were retrieved from European Strong Motion Database, briefly ESM, (Luzi et al., 2016; ESM, 2021) and Italian ACcelerometric Archive, herein ITACA, (Luzi et al., 2019). In detail, data regarding the Central Italy earthquake occurred on the 2016 and recorded by temporary network named 3A have been archived only in the ITACA database (ITACA, 2021). It is worth noting that Greek and Turkish seismic events data were collected to consider earthquake characterised by M value greater than 6.5 and up to 7.6. Moreover, earthquake characterised by H, R, and \log_{10} PGA value greater than 30 km, 400 km, and 2 (cm/s²), respectively, were selected. It should be noted that the ITACA and ESM selected data consider the shallow active crustal region (i.e., SACR zone characterised by shallow events, $H < 35$ km, in agreement to Michelini et al., 2019). The distributions of seismological data of the chosen events are shown in Figs. 2 and 3. The same figures also show the distribution of data described in the next part of this section.

Geophysical data

Dynamic site condition was described by means of the time-averaged shear-wave velocity (V_s) to a depth of 30 meters, the V_{s30} parameter. It is worth noting that the V_{s30} parameter has been successfully adopted to gauge lithostratigraphic effect on seismic wave propagation by Falcone et al. (2021). V_{s30} data (i.e., input data in ML approach), determined by means of *in situ* investigations, are also archived in the ESM and ITACA databases. V_{s30} values were retrieved from Mori et al. (2020a) for ESM and ITACA sites not characterised by *in situ* surveys. Fig. 2 shows the distribution of the V_{s30} data. The V_{s30} map proposed by Mori et al. (2020a), based on SM studies, was adopted here. The SM studies have been carried out for the Italian municipalities through the funds allocated after the 2009 L'Aquila earthquake, in the framework of the Italian program for seismic risk prevention and mitigation (Moscatelli et al., 2020a). Approximately 4,000 SM studies have been already planned, representing about 99.8% of the municipalities eligible for funding (i.e., having 475 years return period $\text{PGA} \geq 0.125\text{g}$). Out of the 4,000 planned SM studies, about 75% have been completed and approved (DPC, 2021). The SM studies permitted to collect, classify, and archive geological, geophysical, and geotechnical data with a uniform approach following national standard criteria (SM Working Group, 2008; TCSM, 2018). The data from *in situ* tests are organised into a

database and georeferenced through an appropriate geographic information system (DPC, 2021). About 35,000 borehole logs and 11,300 V_s profiles, related to about 1,700 Down-Hole and 9,600 MASW tests, were extracted from the SM dataset. Starting from the 11,300 V_s profiles, V_{s30} values were calculated. Mori et al. (2020b) derive a large-scale V_{s30} map for Italy, starting from the global morphological classes after Iwahashi et al. (2018), by integrating the large amount of data from the Italian SM dataset. The V_{s30} map by Mori et al. (2020a) was used here to integrate data where site-specific information was not available.

Morphological data

The morphological elevation h (i.e., an input morphological datum) was retrieved by the Advanced Land Observing Satellite (ALOS) World 3D-30m (herein AW3D30) digital elevation model (DEM). The free version of the DEM (ALOS, 2021) adopted here has 1 arcsec resolution, which is equivalent to approximately 30 m at the Equator. AW3D-30m global DEM data were produced using the data acquired by the Panchromatic Remote Sensing Instrument for Stereo Mapping operated on the ALOS from 2006 to 2011. The Japan Aerospace Exploration Agency, that is the operator of the satellite, produced the global DEM using approximately 3 million images. Considering that AW3D30 model is the digital surface model which represents the canopy top and building roofs' elevations, Caglar et al. (2018) found that AW3D30 is the most accurate DEM among other similar data elevation products freely available. In detail, it was shown that the AW3D30 root mean square error is equal to 1.78 m.

Finally, a GRASS GIS command *r.slope.aspect* (<https://grass.osgeo.org>) was used to generate the other morphological proxies (i.e., h_x , h_y , h_{xx} , and h_{yy}). Such command generates raster maps of first and second order partial derivatives from a raster map of true elevation values (i.e., AW3D30 data in this study). Fig. 2 shows the distribution of the selected morphological data.

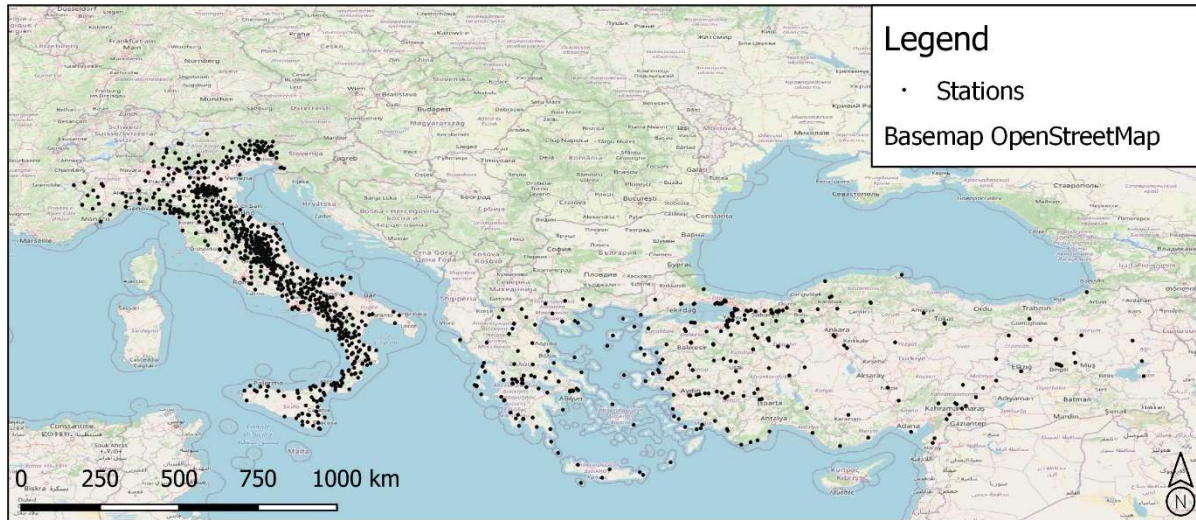


Figure 1. Location of selected dataset (i.e., 1,435 accelerometric stations).

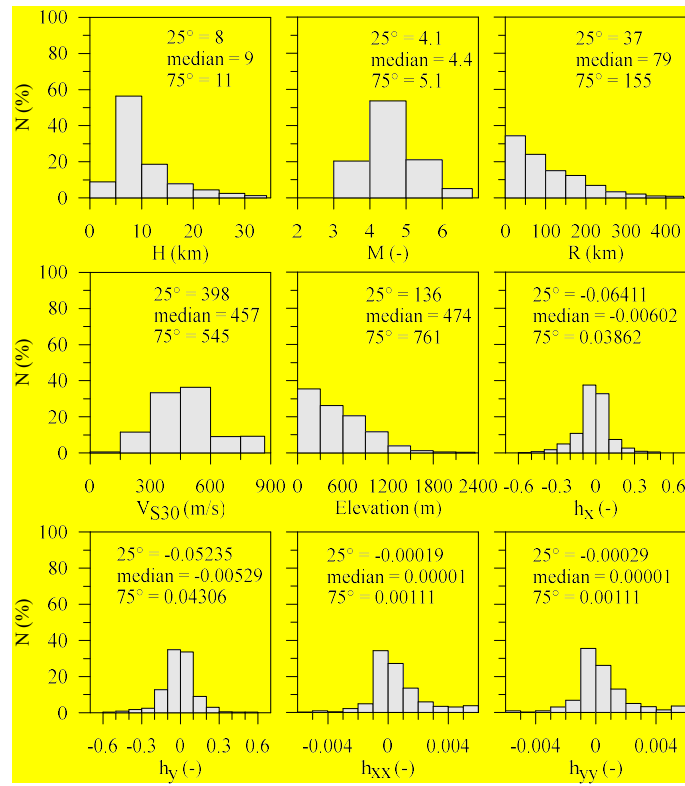


Figure 2. Distribution of input data for the training dataset.

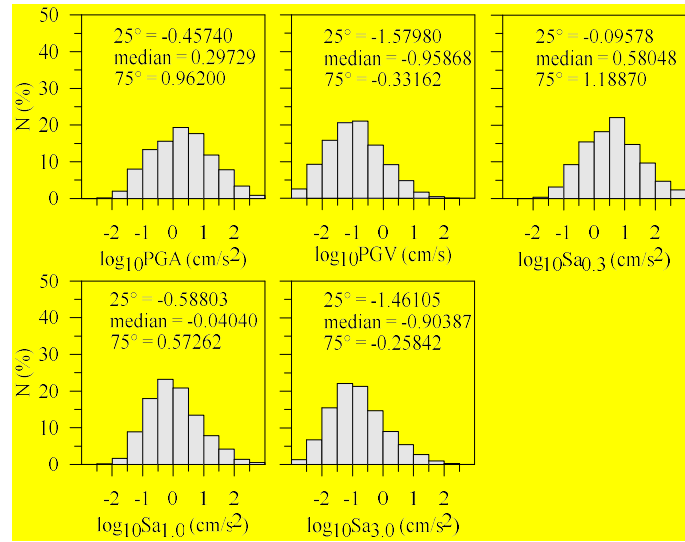


Figure 3. Distribution of output data for the training dataset in terms of geoH IMs.

170 3 Method

171 The “Matlab Regression Learner App” tool (<https://it.mathworks.com/help/stats/regression-learner-app.html>) was employed
172 to produce ground motion prediction maps using a supervised ML approach. With this application, users can choose the desired
173 models among many different methods to automatically train and validate regression models. After training multiple models,
174 they can be compared to choose the best one. The application includes commonly used regression methods such as linear
175 regression models, decision trees, support vector machines, ensembles of tree models, and Gaussian Process Regression (GPR).
176 Fig. 4 shows the adopted ML workflow. After having imported and selected the data (input variables and output variables),
177 the training and validation phases begin. In these phases the ML model that will be used is "adapted" or rather the algorithm
178 is adapted to the training dataset. One of the objectives of this phase is the tuning of the model, acting on the hyperparameters
179 (parameters whose value is used to control the learning process) of the algorithm to minimize errors. The K-fold cross-
180 validation technique was used in this work. The models included in “Matlab Regression Learner App” tool have all been tested.
181 The fitting performance (in term of RMSE) on the validation set was considered as an indicator for the generalization ability
182 of models. Among the available models the best fitting performance in terms of RMSE was provided by the GPR model with
183 exponential kernel (Table 2). GPR is a nonparametric, Bayesian approach to regression, which provides uncertainty
184 measurements on the predictions.
185 The second step is to test the model with the best performance (GPR with exponential kernel in this research) adopting a
186 dataset not included in the training and validation phases. The dataset for the 30 October 2016 seismic event was used since
187 the accelerometric data of many accelerometric stations are available. The test is used to evaluate the accuracy of the model in
188 terms of residuals (Eq. 1). In the workflow of Fig. 4 there is also a phase (comparison) that is not part of the standard ML
189 methodology. The comparison with the ground shaking obtained by completely different methodologies was used to further
190 analyse the ML model in terms of ground motion resolution and variability.
191 Training and cross-validation phases are described in § 3.1. Comparison in terms of residuals with the performance of the
192 existing methods (i.e., an external test) is presented in § 3.2. The comparison with the ground shaking obtained by completely
193 different methodologies is presented in § 4.
194 Moreover, a detailed description of GPR method is outside the scope of this work. Suggested references for comprehensive
195 descriptions of the GPR method are Rasmussen and Williams (2006) and chapter 6 of MathWorks (2019). The above-
196 mentioned k-fold cross-validation (k=5) method is described in chapter 24 of Mathworks (2019).

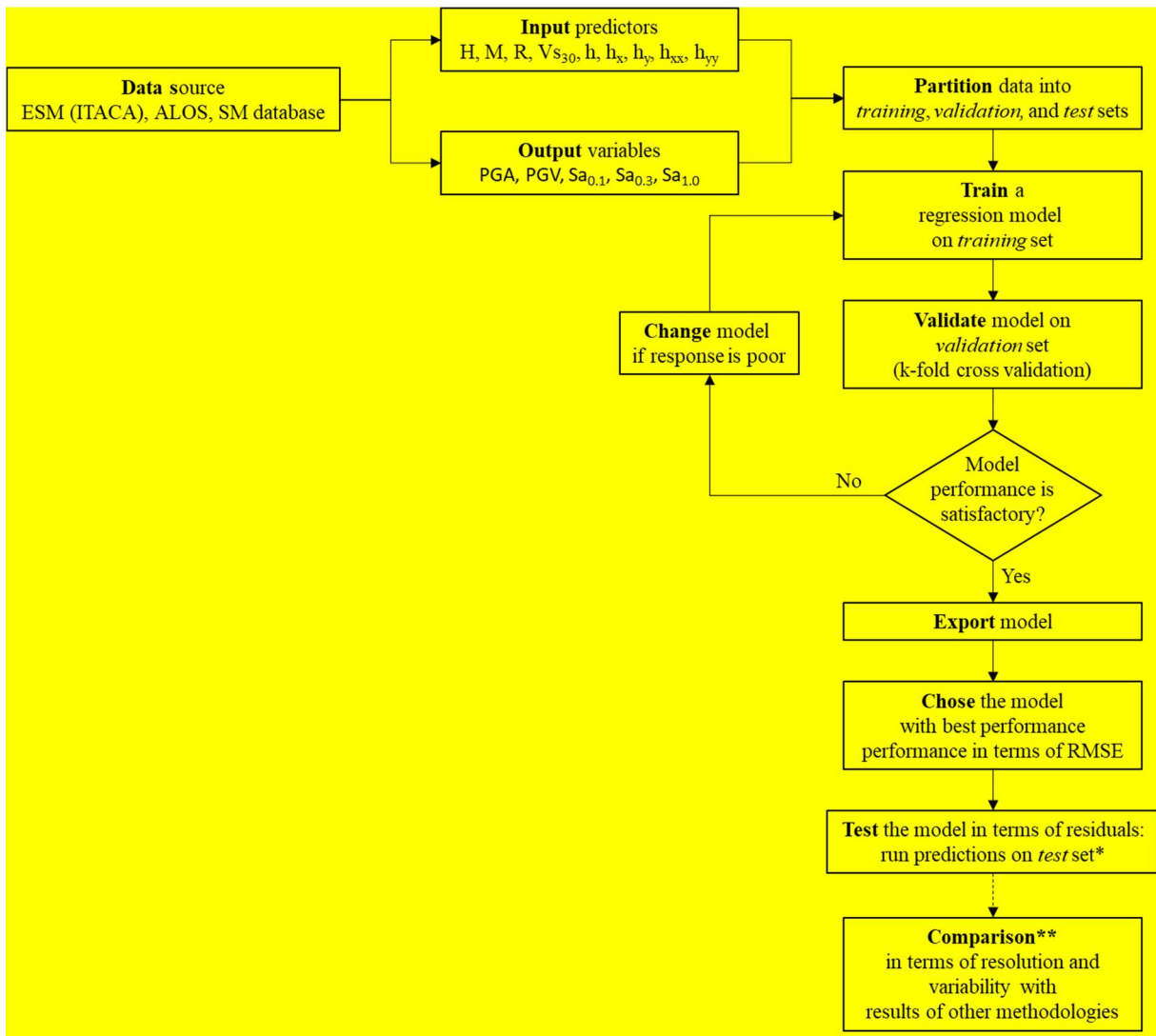


Figure 4. ML workflow adopted in this study.

*The selected test set was the input and output data for the October 30, 2016 seismic event.

** This element of the workflow is not part of the standard ML methodology. This element was introduced to enlighten the capability of the adopted ML procedure in estimating local scale ground motion variability. Comparison against predictions from ShakeMap and 2D numerical simulations was based on August 24, 2016 seismic event input and output data.

3.1 Training and validation phases

The mean RMSE of the five cross-validation datasets were adopted to select the best ML approach. With reference to the tested ML approaches, Table 2 lists the RMSE values for each predicted IM.

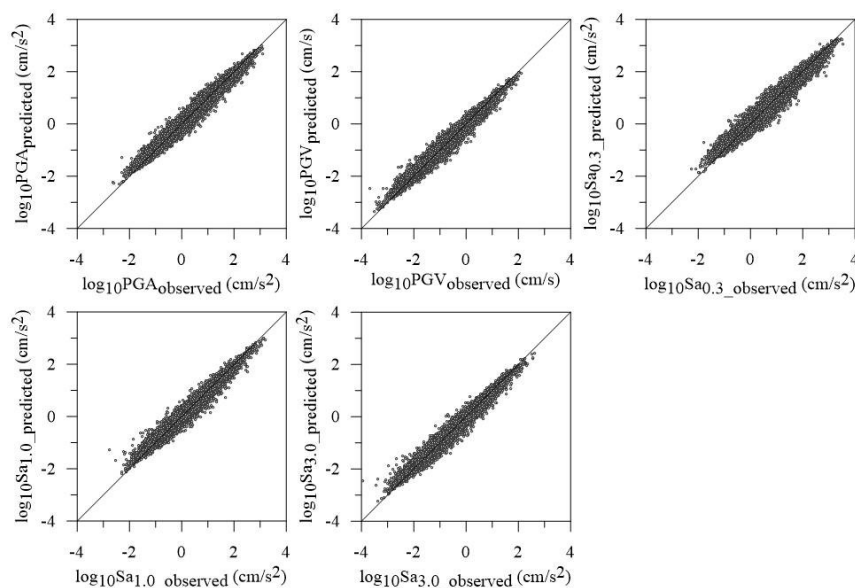
209
210

Table 2. RMSE, for all ML prediction models used to forecast log10 geometric horizontal mean (geoH) of PGA, PGV, and Sa at 0.3 s, 1.0 s, and 3.0 s. Suggested reference for comprehensive descriptions of the ML prediction models is MathWorks (2019).

ML Prediction Model	Performance in term of RMSE				
	PGA	PGV	Sa(0.3s)	Sa(1.0s)	Sa(3.0s)
Linear Regression (Linear)	0.53	0.47	0.50	0.44	0.43
Linear Regression (Interactions Linear)	0.48	0.43	0.47	0.42	0.40
Linear Regression (Robust Linear)	0.53	0.47	0.50	0.44	0.43
Stepwise Linear Regression (Stepwise Linear)	0.48	0.43	0.47	0.42	0.40
Tree (Fine Tree)	0.42	0.38	0.42	0.39	0.38
Tree (Medium Tree)	0.40	0.36	0.40	0.38	0.36
Tree (Coarse Tree)	0.40	0.36	0.40	0.37	0.36
Support Vector Machine (Linear)	0.53	0.48	0.49	0.44	0.43
Support Vector Machine (Quadratic)	0.43	0.39	0.42	0.39	0.39
Support Vector Machine (Cubic)	0.40	0.36	0.40	0.37	0.36
Support Vector Machine (Fine Gaussian)	0.48	0.46	0.48	0.45	0.46
Support Vector Machine (Medium Gaussian)	0.37	0.34	0.38	0.35	0.34
Support Vector Machine (Coarse Gaussian)	0.43	0.39	0.42	0.39	0.38
Ensemble (Boosted Trees)	0.40	0.36	0.40	0.37	0.36
Ensemble (Bagged Trees)	0.33	0.31	0.33	0.31	0.31
Gaussian Process Regression (Squared Exponential)	0.38	0.35	0.39	0.36	0.35
Gaussian Process Regression (Matern 5/2)	0.37	0.34	0.38	0.34	0.34
Gaussian Process Regression (Exponential)	0.31	0.30	0.33	0.30	0.29

211
212
213
214

Referring to the best prediction model (i.e., GPR with exponential kernel) and to the training dataset, Fig. 5 shows the comparison between predicted and observed values.



215
216
217

Figure 5. Comparison between observed and predicted values referring to the output data (i.e., geoH in terms of PGA, PGV, Sa0.3, Sa1.0, and Sa3.0).

The performance of the GPR model is also presented in terms of mean value and standard deviation of the residuals' distributions (Table 3), where the residual is defined according to the Eq. (1) in agreement to what presented by other researchers (Bindi et al., 2011; Jozinović et al., 2021; Michelini et al., 2019). It should be noted that mean and standard deviation of the residuals' distributions referred to ShakeMap and GMPE were retrieved from the work of Jozinović et al. (2021) to evaluate the performance of the ML approach suggested in this study. It is worth noting that the suggested ML approach provide the best performance with respect to the approaches proposed by the other studies in terms of both accuracy (mean value) and precision (standard deviation). In detail, the standard deviation values are reduced by the 45-60%.

$$\text{residual} = \log_{10} \left(\frac{\text{IM}_{\text{observed}}}{\text{IM}_{\text{predicted}}} \right) \quad (1)$$

Table 3. Referring to the training dataset (15,779 data for each IM), comparison of mean and standard deviation values of the residuals' distributions obtained in this study and that reported by other works (geoH stays for geometric mean of the horizontal components).

IM (geoH)	This study (ML)		ShakeMap		GMPE	
	mean	std	mean	std	mean	std
PGA	-0.000033	0.161	0.038	0.372	0.017	0.352
PGV	-0.000015	0.156	0.041	0.380	-0.151	0.330
Sa _{0.3}	0.000024	0.192	0.046	0.370	-0.252	0.359
Sa _{1.0}	0.000028	0.160	0.017	0.374	-0.198	0.303
Sa _{3.0}	-0.000072	0.159	-0.012	0.404	0.083	0.368

3.2 Testing phase

Input and output data for the October 30, 2016 seismic events were selected as external test dataset not included in the training data. The seismic events in Central Italy of 2016 and 2017, began in August 2016 with epicentres located between Latium, Marche, and Umbria Regions. The first strong shock occurred on August 24, 2016, at 3:36 a.m. and had a magnitude of 6.0, with its epicentre located along the Tronto River valley, between the small municipalities of Accumoli and Arquata del Tronto. Two powerful replicas took place on October 26, 2016, with epicentres on the Umbria-Marche border, the first shock with magnitude 5.4 and the second with magnitude 5.9. On October 30, 2016, the strongest quake was recorded, with a moment magnitude of 6.5 with its epicentre in Umbria Region. On January 18, 2017, a new sequence of four strong tremors with a magnitude greater than 5 (with a maximum of 5.5) and epicentres located in Abruzzi Region took place. This set of events caused a total of about 41,000 displaced persons, 388 injured, and 303 deaths.

In detail, the paper refers to the October 30, 2016 mainshocks since according to the available data much more accelerometric data are available and it is therefore possible to make more detailed and reliable analyses.

Mean and std values of the residuals' distributions are presented in this section for the seismic event occurred on October 30, 2016 (briefly named test event), because it is the event with the most recordings of the whole dataset (241 accelerometric stations). It is worth noting that this event was not included in the dataset adopted for the training phase of the ML approach. Noting that 943 seismic events were characterised by $M \leq 6$ and 25 earthquakes by $M > 6$ (see Fig. 3 for the to the training dataset), the Central Italy earthquake occurred on October 30, 2016 ($M = 6.5$) provides a robust test of the adopted ML approach. The GMPE proposed by Bindi et al. (2014) (hereafter also Bindi GMPE) was selected to estimate the IMs at the 241 sites of interest aiming to compare the GMPE and this ML approach performances. It should be noted that the Bindi GMPE provide IMs depending on the V_{S30} as in this study. Furthermore, the OPENQUAKE software (Pagani et al., 2014) was used to determine the IMs values based on the selected GMPE.

Mean and std values regarding the test event (Table 4), are higher than those referred to the training and validation phase (Table 3), as expected, because the GPR model is trained on a few events with high magnitudes as discussed in § 2.

Moreover, mean and std values obtained in this example are lower than those obtained by means of GMPE as shown in Table 4. In detail, the standard deviation values are reduced by the 20-30%. Therefore, the overall performance of the proposed ML approach is satisfactory also at the highest magnitude.

Table 4. Comparison of mean and standard deviation values of the residuals' distributions obtained in this study and by means of GMPE (Bindi et al., 2014), regarding the earthquake occurred on October 30, 2016, (241 data for each IM; geoH stays for geometric mean of the horizontal components).

IM (geoH)	This study		GMPE	
	mean	std	mean	std
PGA	0.0019	0.30	-0.19	0.43
PGV	0.0130	0.34	-0.16	0.42
Sa _{0.3}	0.0170	0.32	-0.18	0.39
Sa _{1.0}	-0.0550	0.35	-0.38	0.46
Sa _{3.0}	-0.0360	0.39	-0.23	0.55

4 Ground motion prediction map

After having demonstrated the goodness of the proposed method to reproduce IM values, this chapter presents examples of predictive maps produced by means of the exponential GPR model with a 50 m x 50 m resolution. In § 4.1 the map for the August 24, 2016 seismic event of Central Italy is produced to compare some significant IM profiles produced with independent

267 advanced numerical simulations and data retrieved from ShakeMaps (2021). In § 4.2 the map of the event of October 30, 2016,
 268 already used for the test phase, is analyzed in terms of spatial correlation structure.

269 **4.1 Ground motion prediction map for August 24, 2016 seismic event of Central Italy and comparison with numerical**
 270 **modelling**

271 The adopted GPR model was used to produce ground motion prediction maps referring to the earthquake occurred on August
 272 24, 2016. The ground motion prediction map of the $Sa_{0.3}$ reported in Fig. 6 is one of the cartographic results of this study; maps
 273 of PGA, PGV, and other spectral ordinates are in the supplementary materials. Macroseismic intensities, I_{MCS} , retrieved by
 274 Galli et al. (2017) are also reported next to the name of the villages in Fig. 6. These maps were chosen because the 0.3 s period
 275 is the fundamental vibration period of most buildings in the area (i.e., 2-3 storey buildings). Moreover, 0.3 s is compatible with
 276 the results of modelling provided by Gaudiosi et al. (2021), Giallini et al. (2020), Grelle et al. (2020) for the same areas.

277 The map of Fig. 6 shows an output that is in good agreement with the geophysical data (i.e., V_{S30} in Fig. 7) and
 278 geomorphological data (i.e., h , h_x , h_y , h_{xx} , h_{yy} not shown here for sake of brevity) and, therefore, highlights local site effects.
 279 In fact, referring to Fig. 6, it can be noted that the highest $Sa_{0.3}$ values well describe the valleys' trend (i.e., the largest and
 280 continuous Tronto River valley) and the two extended areas in the southern part of the map (i.e., near Petrana and Torrita
 281 villages), which are characterized by lowest values of V_{S30} (Mori et al., 2020a). Fig. 8 shows the ShakeMap of $Sa_{0.3}$ regarding
 282 the Central Italy earthquake occurred on August 24, 2016 for the same area sketched in Fig. 6. As a general issue referring to
 283 the ShakeMaps, the higher the distance from the epicentre (the star in Fig. 8) and the lower the predicted $Sa_{0.3}$. Hence, the
 284 ShakeMaps does not provide ground motion variability induced by the local site condition (i.e., sub-soil setting and
 285 topography). In detail, ShakeMap provides $Sa_{0.3}$ equal to 0.36 g for the entire area of Arquata del Tronto (square A in Fig. 8)
 286 and equal to 0.99 and 1.08 g for Amatrice (square B in Fig. 8).

287 Referring to A and B close-ups of Fig. 6, Fig. 9 shows the mean values of $Sa_{0.3}$ in the left side and the standard deviation, std,
 288 values in the right side. It should be noted that the uncertainty is provided by a combination of the input data values. The
 289 uncertainty increases referring to input data values for which the ML is not well trained (Figs. 2 and 3 and discussion in § 2).
 290 For instance, std values around 0.3-0.4 are in the areas of inhabited villages, characterised by input data values widely
 291 represented in the training dataset, while values in the range 0.6-0.8 are observed in correspondence with the combination of
 292 high slope values and high V_{S30} values, which are underrepresented in the training dataset.

293 In addition to the maps, Fig. 10 shows the profiles (2 at Amatrice and 1 at Arquata del Tronto) of Sa at 0.3 s and the comparison
 294 with the values of the same shaking parameter, calculated with different methodological approaches: ground motion prediction
 295 with ML approach (this study), 2D numerical simulations (modified after Gaudiosi et al., 2021; Giallini et al., 2020; Grelle et
 296 al., 2020), and ShakeMap (2021). All the models are defined for the geometric mean (geoH) of the horizontal components. As
 297 ShakeMaps are released for the maximum of the horizontal components, the ShakeMap values are converted to geoH according
 298 to the empirical relation proposed by Beyer and Bommer (2006). The three profiles were chosen because they represent three
 299 very different geological and geomorphological structures: narrow valley (section AA' in Fig. 10, Arquata del Tronto), plateau

300 of soft ground (section BB' in Fig. 10, Amatrice), morphology of a mountain peak with coverage of soft ground (section CC'
301 in Fig. 10, close to Amatrice). As a matter of fact, the adopted ML approach reproduces the so-called valley effect, as in the
302 case of Arquata del Tronto shallow valley (see the trend for $200 \leq x \leq 400$ m in AA'), the combined lithostratigraphic and
303 topographic effects, as in the case of Amatrice village (see the trend for $200 \leq x \leq 500$ m in BB'), and the topographic
304 amplification, as in the case of the AMT accelerometric station (Luzi et al., 2019; see the trend for $100 \leq x \leq 200$ m in CC'). It
305 should be noted that the trend of the values of our study reproduces that of the numerical simulations, also getting closer to the
306 recorded values at Osservatorio Sismico delle Strutture (OSS, a network of buildings and bridges monitored *in continuum* by
307 the Italian Civil Protection Department) site and AMT station (stars in BB' and CC'). Moreover, the profiles provided by the
308 ML approach are much more articulated and complex than the constant value (horizontal dashed line) of the ShakeMap, which
309 obviously fails to grasp the local site effects at this scale.
310

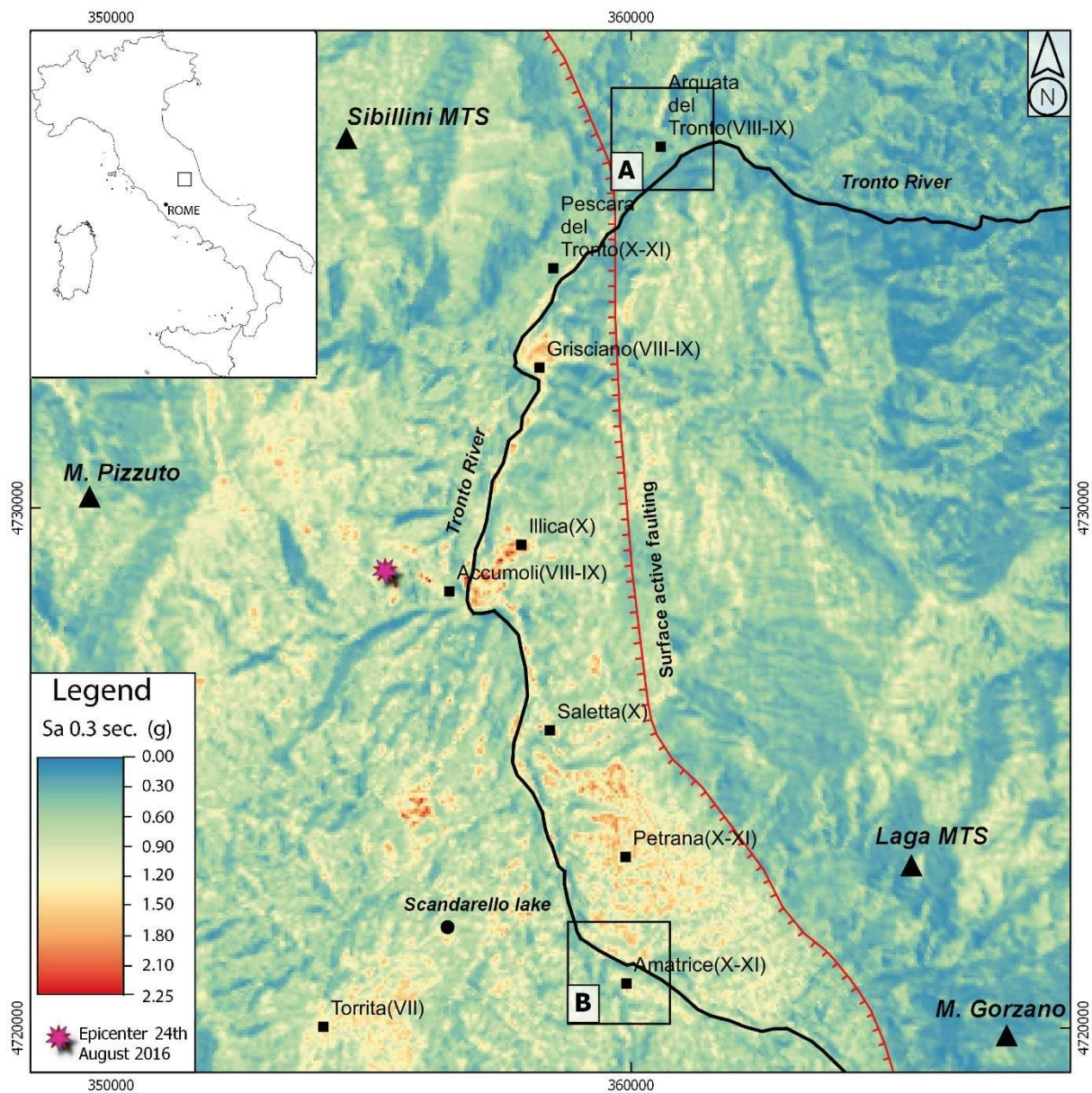


Figure 6. Ground motion prediction map of $Sa_{0.3}$ (resolution 50 m x 50 m) regarding the Central Italy earthquake occurred on August 24, 2016. I_{MCS} values retrieved by Galli et al. (2017) are reported next to the name of the villages. A and B squares are referred to the close ups at Arquata del Tronto and Amatrice, respectively. The surface active faulting, sketched in the figure, has been slightly modified after Galli et al. (2017).

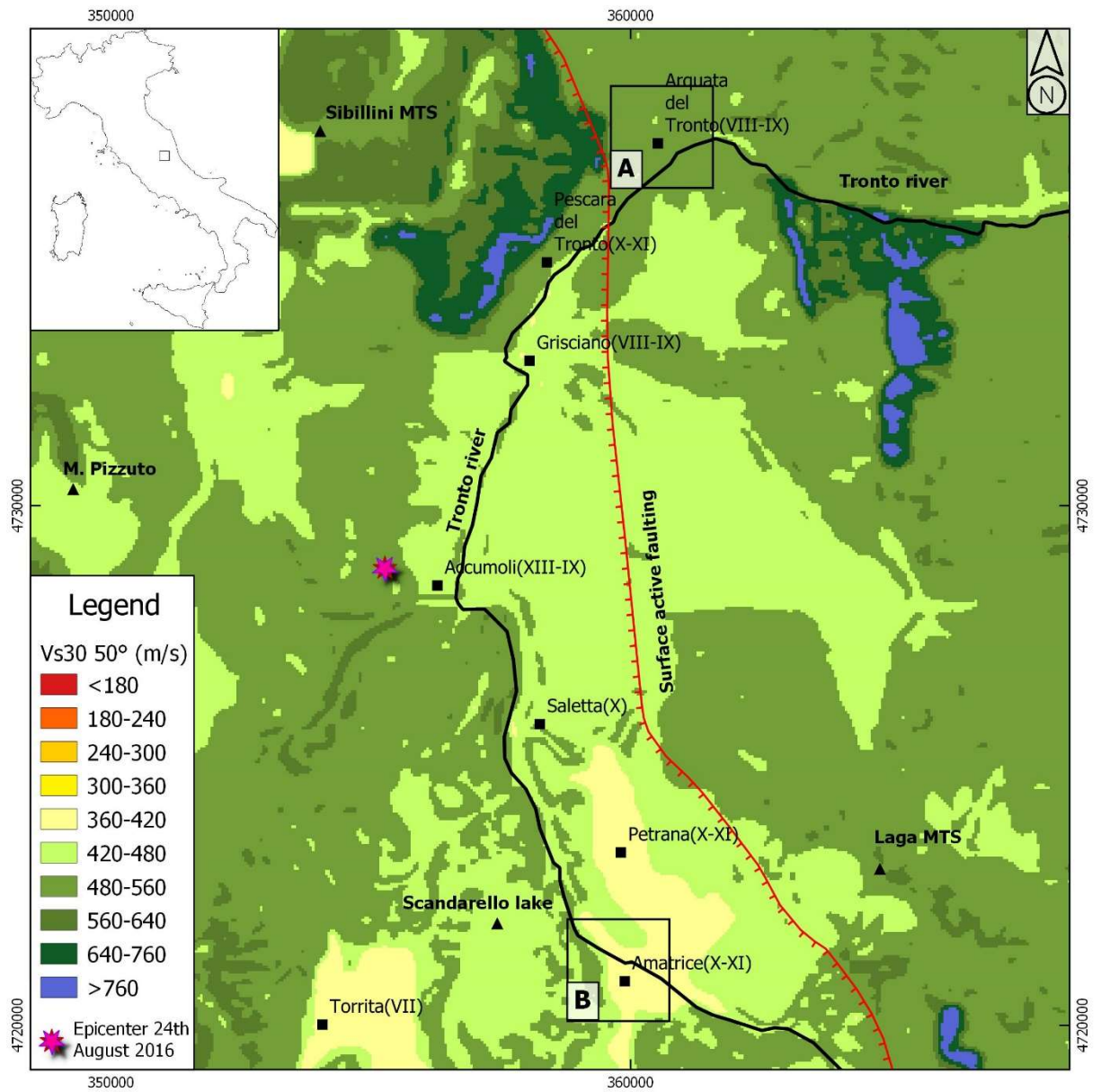


Figure 7. V_{s30} maps for the area of interest shown in Fig. 6. It can be noted that two extended areas in the southern part of the map (i.e., near Petrana and Torrita villages) are characterized by lowest values of V_{s30} inducing the highest $S_{a0.3}$ values (i.e., valley effect) as shown in Fig. 6.

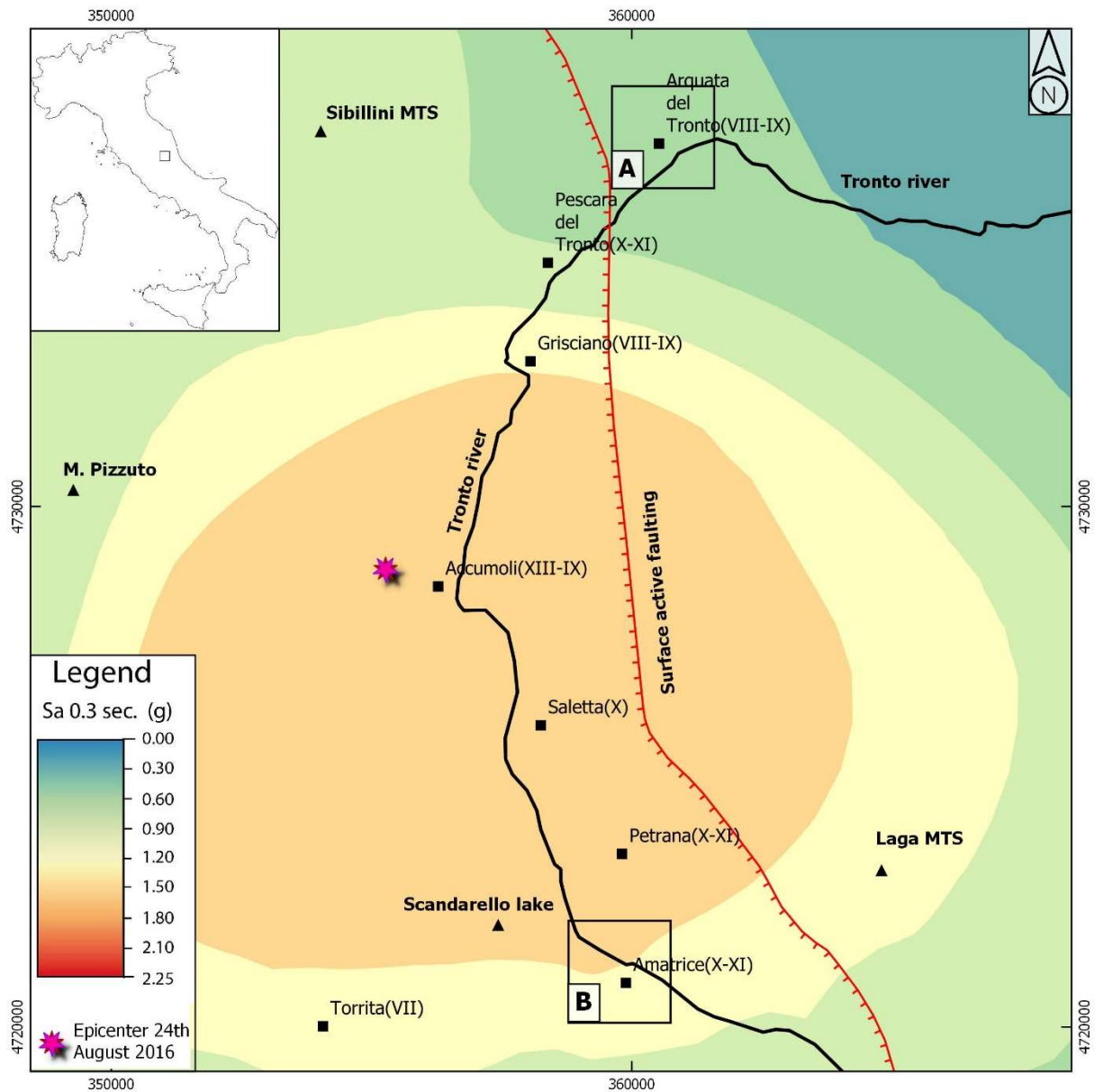


Figure 8. ShakeMap (slightly modified from ShakeMap, 2021) of $Sa_{0.3}$ regarding the Central Italy earthquake occurred on August 24, 2016. A and B squares are referred to the close-ups at Arquata del Tronto and Amatrice, respectively. From the centre of the figure to the border, the homogenous coloured areas correspond to 1.20-1.50 g, 0.90-1.20 g, 0.60-0.90 g, 0.30-0.60 g, and 0.01-0.30 g intervals. It is evident that the map does not capture the variability at short distances

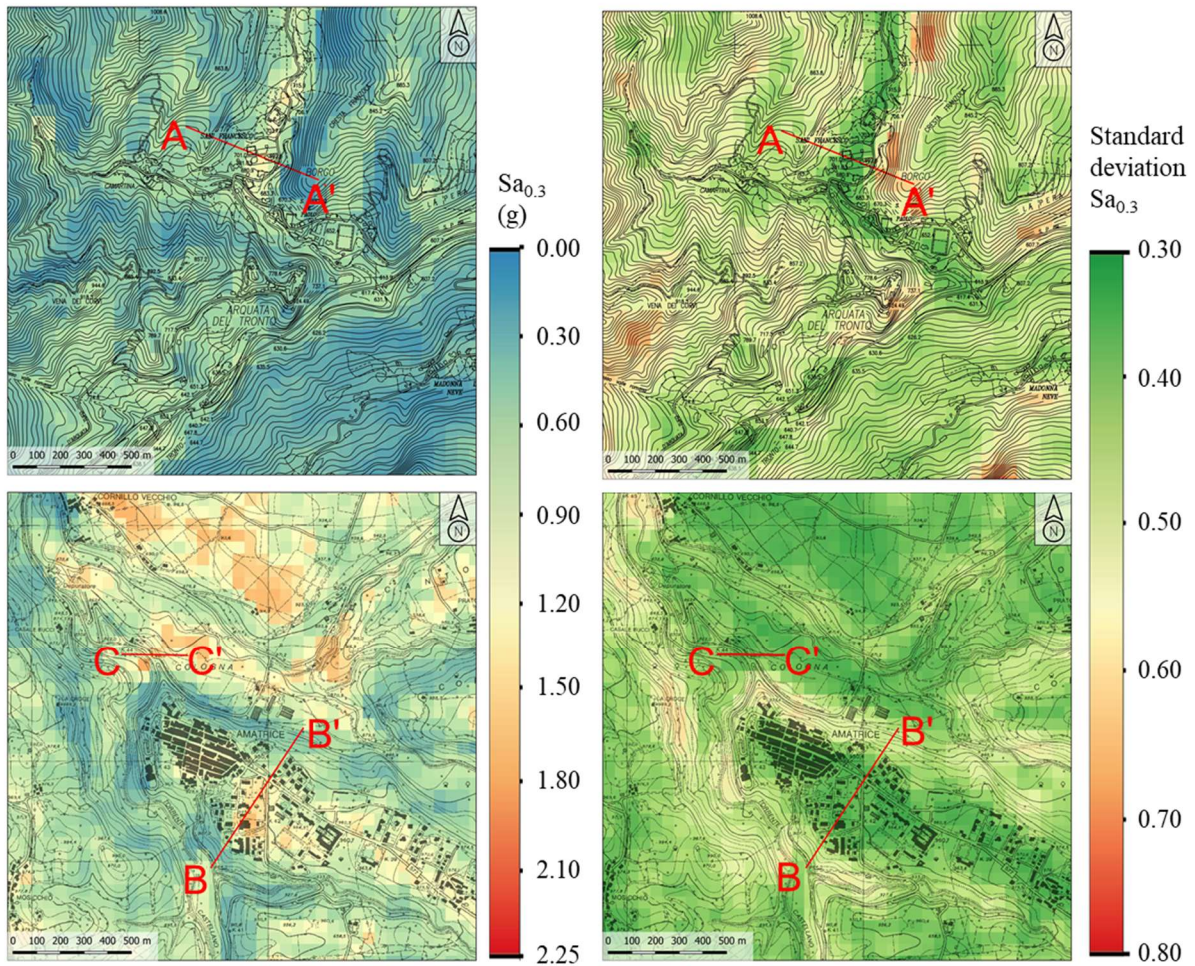


Figure 9. Ground motion prediction maps (Central Italy earthquake occurred on August 24, 2016) regarding the Arquata del Tronto (top) and Amatrice (bottom) in terms of $Sa_{0.3}$ mean value (left) and standard deviation (right) (resolution 50 m x 50 m). The base topographic layer was retrieved from Regione Marche (2021) and Regione Lazio (2021) for Arquata del Tronto and Amatrice. The uncertainty estimation is available here: <https://it.mathworks.com/help/stats/gaussian-process-regression-models.html>.

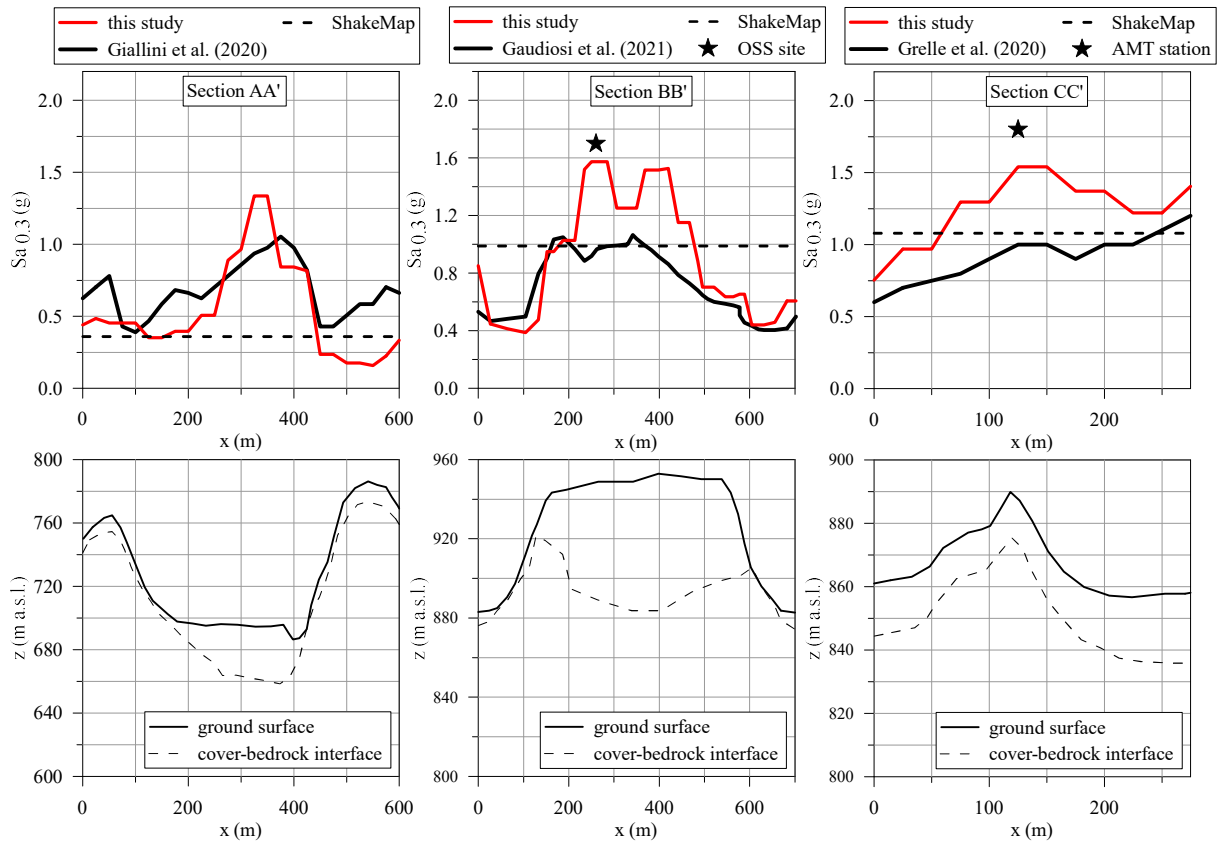


Figure 10. Profiles of $Sa_{0.3}$ (top) for Central Italy earthquake occurred on August 24, 2016 and simplified sub-soil sections (bottom) of Arquata del Tronto (Section AA') and Amatrice (Sections BB' and CC'). Cross sections' locations are in Fig. 9. $Sa_{0.3}$ profiles and geological information retrieved and modified after Gaudiosi et al. (2021), Giallini et al. (2020), Grelle et al. (2020); ShakeMap (2021). The black stars indicate values recorded at the OSS site and AMT station (for details see the text).

Discussion and conclusions

Intensity and frequency contents of ground motions can be altered by many factors. Up until now, numerous empirical models of ground motion amplification have been developed based on conventional regression analyses, considering few key factors such as intensity measures of rock motions, shear wave velocities of soils, and territory morphology. Since Machine Learning techniques have been applied to many fields, this work investigated on efficacy of using such techniques for developing models to predict ground motion over large areas with a 50 m resolution raster.

A set of about 16,000 ground motion data from Italian and European networks were adopted to train a Gaussian Process Regression model, while recordings by 241 stations of the seismic events occurred in Italy on October 30, 2016 were used to test the same model. Peak ground acceleration and velocity, and spectral acceleration at 3 periods (i.e., 0.3, 1, and 3 s) were compared to the recorded data allowing to obtain residuals. With reference to the training dataset, mean value and standard deviation of the residuals' distribution were found equal to about 0 and to about 0.1, respectively. With reference to the test

348 dataset characterised by magnitude equal to 6.5, mean value and standard deviation of the residuals' distribution were found
349 equal to 0.01 and 0.3, respectively. Hence, the performance of the adopted Machine Learning technique was confirmed
350 satisfactory also for magnitude higher than 6.

351 In addition, maps of ground motion in terms of peak ground acceleration, peak ground velocity, and of spectral acceleration at
352 the selected three periods were produced for the Central Italy seismic event occurred on August 24, 2016. Profiles of intensity
353 measures were in satisfactory agreement with those obtained by means of advanced numerical simulations of seismic site
354 response referring to the same seismic event. Moreover, the adopted Machine Learning approach greatly improves the
355 performance of existing methods.

356 Three main novelties of the work are synthesized in the following:

- 357 1) forecast of ground motion with high resolution (i.e., a 50 m x 50 m raster), in agreement with results of local scale numerical
358 modelling. This outcome is achieved by means of Machine Learning techniques and large datasets including
359 morphological, geological, geophysical, and geotechnical features (mainly the seismic microzonation dataset; DPC, 2021).
360 Moreover, about 1,000 seismic events recorded by 1'435 accelerometric stations (ESM, 2021; ITACA, 2021) were
361 analysed. The Machine Learning approach combines morphological and subsurface proxies: elevation, first and second
362 order topographic gradient (define the morphological characteristics of the territory), mean shear wave velocity in the upper
363 30 m (defines the dynamic response of a site as induced by the subsoil condition). Magnitude, epicentral, and hypocentral
364 distances provide the source conditions;
- 365 2) use of robust statistical techniques such as Gaussian Process Regression. Among the machine learning based models, the
366 model developed by the regression and Gaussian approach provides the best performance in terms of both precision and
367 accuracy, that are standard deviation and mean value of the residuals' distribution, respectively.

368 In terms of applications, the ground motion maps generated by means of the proposed Machine Learning approach are useful
369 both for urban planning (aimed at reducing seismic risk) and for emergency management (aimed at a *near real time* estimation
370 of damage to buildings and infrastructures). With reference to the emergency phase, by knowing the position and depth of the
371 hypocentre and the magnitude of the event (in Italy these data are available a few minutes after the event), it is possible to
372 predict the losses in the area struck by the earthquake in near real time. Overall, considering that the paradigm should be shifted
373 from managing disasters to managing risk, the proposed methodology could represent a key-tool in seismic risk mitigation
374 strategies deployed both pre and post seismic event.

375 In conclusion, the research on this topic will continue and focus on specific goals, which are listed in the following:

- 376 - improve the method with more input proxies, made available after the seismic microzonation project for the whole national
377 territory. In detail, maps of the depth to the engineering bedrock and of the fundamental frequency of the deposit will be soon
378 available and allow to use such parameters as input data for the Machine Learning approach;
- 379 - improve the method with worldwide seismological dataset;
- 380 - improve the spatial resolution of existing input proxies integrating remote sensing data;

381 - improve the spatial correlation analysis.

382 **Author contributions**

383 Conceptualization: FM, GA. Data curation: FM, AM, RS. Formal analysis: FM, RS. Funding acquisition: MM. Methodology:
384 FM, AM, GF, GA, RS, MM, GN. Project administration: MM. Supervision: FM, MM, GN. Validation: FM, AM, GF, GA.
385 Visualization: AM, GF. Writing – original draft preparation: FM, GF, GN. Writing – review & editing: FM, AM, GF, GA,
386 RS, MM, GN.

387 **Competing interests**

388 The authors declare that they have no conflict of interest.

389 **Acknowledgements**

390 Authors would like to thank F. Bramerini, S. Castenetto, A. Gorini and D. Spina, (Italian Department for Civil Protection), for
391 the useful discussions. We also thank S. Giallini and I. Gaudiosi (both from CNR IGAG, Italy) for providing the ground motion
392 data obtained by means of numerical simulation for Amatrice and Arquata del Tronto areas (Italy).

393 **Financial support**

394 This research was supported by the Presidency of the Council of Ministers, Italian Department for Civil Protection, in the
395 framework of the project “Contratto concernente l’affidamento di servizi per il programma per il supporto al rafforzamento
396 della Governance in materia di riduzione del rischio sismico e vulcanico ai fini di protezione civile nell’ambito del PON
397 Governance e Capacità Istituzionale 2014–2020 - CIG6980737E65” (M. Moscatelli scientific coordinator for CNR).

398 **References**

399 ALOS. Viewed May 2021. < <http://www.eorc.jaxa.jp/ALOS/en/aw3d30/>>, 2021.

400 Beyer, K. and Bommer, J. J.: Relationships between Median Values and between Aleatory Variabilities for Different
401 Definitions of the Horizontal Component of Motion, Bull. Seismol. Soc. Am., 96(4A), 1512–1522, doi:10.1785/0120050210,
402 2006.

403 Bindi, D., Pacor, F., Luzi, L., Puglia, R., Massa, M., Ameri, G. and Paolucci, R.: Ground motion prediction equations derived
404 from the Italian strong motion database, Bull. Earthq. Eng., 9(6), 1899–1920, doi:10.1007/s10518-011-9313-z, 2011.

405 Bindi, D., Massa, M., Luzi, L., Ameri, G., Pacor, F., Puglia, R. and Augliera, P.: Pan-European ground-motion prediction
 406 equations for the average horizontal component of PGA, PGV, and 5%-damped PSA at spectral periods up to 3.0 s using the
 407 RESORCE dataset, *Bull. Earthq. Eng.*, 12(1), 391–430, doi:10.1007/s10518-013-9525-5, 2014.

408 Bouckovalas, G. D. and Papadimitriou, A. G.: Numerical evaluation of slope topography effects on seismic ground motion,
 409 *Soil Dyn. Earthq. Eng.*, 25(7–10), 547–558, doi:10.1016/j.soildyn.2004.11.008, 2005.

410 Brando, G., Pagliaroli, A., Cocco, G. and Di Buccio, F.: Site effects and damage scenarios: The case study of two historic
 411 centers following the 2016 Central Italy earthquake, *Eng. Geol.*, 272, 105647, doi:10.1016/j.enggeo.2020.105647, 2020.

412 Caglar, B., Becek, K., Mekik, C. and Ozendi, M.: On the vertical accuracy of the ALOS world 3D-30m digital elevation model,
 413 <https://doi.org/10.1080/2150704X.2018.1453174>, 9(6), 607–615, doi:10.1080/2150704X.2018.1453174, 2018.

414 Chilès, J.P. and Delfiner P.: *Geostatistics: modeling spatial uncertainty*, 2nd edn. Wiley, Hoboken, p 726. ISBN 978-0-470-
 415 18315-1, 2012.

416 DPC, Dipartimento della Protezione Civile: Commissione tecnica per il supporto e monitoraggio degli studi di Microzonazione
 417 Sismica (ex art.5, OPCM3907/10) – WebMs; WebCLE. A cura di: M. S. Benigni, F. Bramerini, G. Carbone, S. Castenetto, G.
 418 P. Cavinato, M. Coltella, M. Giuffrè, M. Moscatelli, G. Naso, A. Pietrosante, F. Stigliano. Viewed May 2021. www.webms.it,
 419 2021.

420 ESM. Viewed May 2021. <<https://esm.mi.ingv.it/>>, 2021.

421 Falcone, G., Boldini, D. and Amorosi, A.: Site response analysis of an urban area: A multi-dimensional and non-linear
 422 approach, *Soil Dyn. Earthq. Eng.*, 109, 33–45, doi:10.1016/J.SOILDYN.2018.02.026, 2018.

423 Falcone, G., Romagnoli, G., Naso, G., Mori, F., Peronace, E. and Moscatelli, M.: Effect of bedrock stiffness and thickness on
 424 numerical simulation of seismic site response. Italian case studies, *Soil Dyn. Earthq. Eng.*, 139, 106361,
 425 doi:10.1016/j.soildyn.2020.106361, 2020a.

426 Falcone, G., Boldini, D., Martelli, L. and Amorosi, A.: Quantifying local seismic amplification from regional charts and site
 427 specific numerical analyses: a case study, *Bull. Earthq. Eng.*, 18(1), 77–107, doi:10.1007/s10518-019-00719-9, 2020b.

428 Falcone, G., Acunzo, G., Mendicelli, A., Mori, F., Naso, G., Peronace, E., Porchia, A., Romagnoli, G., Tarquini, E. and
 429 Moscatelli, M.: Seismic amplification maps of Italy based on site-specific microzonation dataset and one-dimensional
 430 numerical approach, *Eng. Geol.*, 289, 106170, doi:10.1016/j.enggeo.2021.106170, 2021.

431 Fayjaloun, R., Negulescu, C., Roullé, A., Auclair, S., Gehl, P., Faravelli, M., Abrahamczyk, L., Petrovčić, S. and Martinez-
 432 Frias, J.: Sensitivity of Earthquake Damage Estimation to the Input Data (Soil Characterization Maps and Building Exposure):
 433 Case Study in the Luchon Valley, France, *Geosci.* 2021, Vol. 11, Page 249, 11(6), 249, doi:10.3390/geosciences11060249,
 434 2021.

435 Galli, P., Castenetto, S. and Peronace, E.: The Macroseismic Intensity Distribution of the 30 October 2016 Earthquake in
 436 Central Italy (Mw 6.6): Seismotectonic Implications, *Tectonics*, 36(10), 2179–2191, doi:10.1002/2017TC004583, 2017.

437 Gatmiri, B. and Arson, C.: Seismic site effects by an optimized 2D BE/FE method II. Quantification of site effects in two-
 438 dimensional sedimentary valleys, *Soil Dyn. Earthq. Eng.*, 28(8), 646–661, doi:10.1016/j.soildyn.2007.09.002, 2008.

439 Gaudiosi, I., Simionato, M., Mancini, M., Cavinato, G. P., Coltella, M., Razzano, R., Sirianni, P., Vignaroli, G. and Moscatelli,
 440 M.: Evaluation of site effects at Amatrice (central Italy) after the August 24th, 2016, Mw 6.0 earthquake, *Soil Dyn. Earthq.*
 441 *Eng.*, 144, 106699, doi:10.1016/j.soildyn.2021.106699, 2021.

442 Gazetas, G.: Vibrational characteristics of soil deposits with variable wave velocity, *Int. J. Numer. Anal. Methods Geomech.*,
 443 6(1), 1–20, doi:10.1002/nag.1610060103, 1982.

444 Giallini, S., Pizzi, A., Pagliaroli, A., Moscatelli, M., Vignaroli, G., Sirianni, P., Mancini, M. and Laurenzano, G.: Evaluation
 445 of complex site effects through experimental methods and numerical modelling: The case history of Arquata del Tronto, central
 446 Italy, *Eng. Geol.*, 272, 105646, doi:10.1016/j.enggeo.2020.105646, 2020.

447 Grelle, G., Gargini, E., Facciorusso, J., Maresca, R. and Madiati, C.: Seismic site effects in the Red Zone of Amatrice hill
 448 detected via the mutual sustainment of experimental and computational approaches, *Bull. Earthq. Eng.*, 18(5), 1955–1984,
 449 doi:10.1007/s10518-019-00777-z, 2020.

450 Iwahashi, J., Kamiya, I., Matsuoka, M. and Yamazaki, D.: Global terrain classification using 280 m DEMs: segmentation,
 451 clustering, and reclassification, *Prog. Earth Planet. Sci.*, 5(1), 1, doi:10.1186/s40645-017-0157-2, 2018.

452 Infantino, M., Smerzini, C. and Lin, J.: Spatial correlation of broadband ground motions from physics-based numerical
 453 simulations, *Earthquake Eng Struct Dyn.* 2021;1–20. [wileyonlinelibrary.com](http://onlinelibrary.wiley.com), 2021.

454 **ITACA. Viewed May 2021. < http://itaca.mi.ingv.it/ItacaNet_30/#/home >, 2021.**

455 Jozinović, D., Lomax, A., Štajduhar, I. and Michelini, A.: Rapid prediction of earthquake ground shaking intensity using raw
 456 waveform data and a convolutional neural network, *Geophys. J. Int.*, 222(2), 1379–1389, doi:10.1093/GJI/GGAA233, 2021.

457 Kim, S., Hwang, Y., Seo, H. and Kim, B.: Ground motion amplification models for Japan using machine learning techniques,
 458 Soil Dyn. Earthq. Eng., 132, 106095, doi:10.1016/j.soildyn.2020.106095, 2020.

459 Kubo, H., Kunugi, T., Suzuki, W., Suzuki, S. and Aoi, S.: Hybrid predictor for ground-motion intensity with machine learning
 460 and conventional ground motion prediction equation, Sci. Rep., doi:10.1038/s41598-020-68630-x, 2020.

461 Luo, Y., Fan, X., Huang, R., Wang, Y., Yunus, A. P. and Havenith, H. B.: Topographic and near-surface stratigraphic
 462 amplification of the seismic response of a mountain slope revealed by field monitoring and numerical simulations, Eng. Geol.,
 463 271, 105607, doi:10.1016/j.enggeo.2020.105607, 2020.

464 Luzi L, Puglia R, Russo E & ORFEUS WG5: Engineering Strong Motion Database, version 1.0. Istituto Nazionale di Geofisica
 465 e Vulcanologia, Observatories & Research Facilities for European Seismology. doi: 10.13127/ESM, 2016.

466 Luzi L, Pacor F, Puglia R: Italian Accelerometric Archive v3.0. Istituto Nazionale di Geofisica e Vulcanologia, Dipartimento
 467 della Protezione Civile Nazionale, doi: 10.13127/itaca.3.0, 2019.

468 Luzi L., Lanzano G., Felicetta C., D’Amico M. C., Russo E., Sgobba S., Pacor, F., & ORFEUS Working Group 5: Engineering
 469 Strong Motion Database (ESM) (Version 2.0). Istituto Nazionale di Geofisica e Vulcanologia (INGV).
 470 <https://doi.org/10.13127/ESM.2>, 2020.

471 Mathworks: Statistics and Machine Learning Toolbox User’s Guide R2019b. The MathWorks Inc. Natick, MA, 2019.

472 Michelini, A., Faenza, L., Lanzano, G., Lauciani, V., Jozinović, D., Puglia, R. and Luzi, L.: The new shakemap in Italy:
 473 Progress and advances in the last 10 yr, Seismol. Res. Lett., 91(1), 317–333, doi:10.1785/0220190130, 2019.

474 Mori, F., Gaudiosi, I., Tarquini, E., Bramerini, F., Castenetto, S., Naso, G. and Spina, D.: HSM: a synthetic damage-constrained
 475 seismic hazard parameter, Bull. Earthq. Eng., 1–24, doi:10.1007/s10518-019-00677-2, 2019.

476 Mori, F., Mendicelli, A., Moscatelli, M., Romagnoli, G., Peronace, E. and Naso, G.: A new Vs30 map for Italy based on the
 477 seismic microzonation dataset, Eng. Geol., 275, 105745, doi:10.1016/j.enggeo.2020.105745, 2020a.

478 Mori, F., Gena, A., Mendicelli, A., Naso, G. and Spina, D.: Seismic emergency system evaluation: The role of seismic hazard
 479 and local effects, Eng. Geol., 270, 105587, doi:10.1016/j.enggeo.2020.105587, 2020b.

480 Moscatelli, M., D. Albarello, G. Scarascia Mugnozza, and M. Dolce: The Italian approach to seismic microzonation, Bull.
 481 Earthq. Eng., 18, 5425–5440, <https://doi.org/10.1007/s10518-020-00856-6>, 2020a.

482 Moscatelli, M., Vignaroli, G., Pagliaroli, A., Razzano, R., Avallè, A., Gaudiosi, I., Giallini, S., Mancini, M., Simionato, M.,
 483 Sirianni, P., Sottili, G., Bellanova, J., Calamita, G., Perrone, A., Piscitelli, S. and Lanzo, G.: Physical stratigraphy and
 484 geotechnical properties controlling the local seismic response in explosive volcanic settings: the Stracciaccia maar (central
 485 Italy), *Bull. Eng. Geol. Environ.*, 1–21, doi:10.1007/s10064-020-01925-5, 2020b.

486 Pagani, M., Monelli, D., Weatherill, G., Danciu, L., Crowley, H., Silva, V., Henshaw, P., Butler, L., Nastasi, M., Panzeri, L.,
 487 Simionato, M. and Vigano, D.: OpenQuake Engine: An Open Hazard (and Risk) Software for the Global Earthquake Model,
 488 *Seismol. Res. Lett.*, 85(3), 692–702, doi:10.1785/0220130087, 2014.

489 Pagliaroli, A., Moscatelli, M., Raspa, G., Naso, G.: Seismic microzonation of the central archaeological area of Rome: results
 490 and uncertainties, *Bull. Earthq. Eng.* 12, 1405–1428. <https://doi.org/10.1007/s10518-013-9480-1>, 2014.

491 Pebesma, E.J.: Multivariable geostatistics in S: the gstat package, *Computers & Geosciences*, 30, 683–691, 2004.

492 Paoletta, L., Spacagna, R.L., Chiaro, G., Modoni, G.: A simplified vulnerability model for the extensive liquefaction risk
 493 assessment of buildings. *Bulletin of Earthquake Engineering*, Volume 19, Issue 10, Pages 3933 – 3961, 2021

494 Pitilakis, K., Raptakis, D., Lontzetidis, K., Tika-Vassilikou, T. and Jongmans, D.: Geotechnical and geophysical description
 495 of euro-seistest, using field, laboratory tests and moderate strong motion recordings, *J. Earthq. Eng.*, 3(3), 381–409,
 496 doi:10.1080/13632469909350352, 1999.

497 R Core Team: R: A language and environment for statistical computing. R Foundation for Statistical Computing, Vienna,
 498 Austria, <https://www.R-project.org/>, 2021.

499 Rasmussen, C. E. and Williams, C. K. I.: *Gaussian Processes for Machine Learning*, MIT Press, ISBN 026218253X,
 500 Massachusetts Institute of Technology, 2006.

501 Raspa G., Moscatelli M., Stigliano F.P., Patera A., Folle D., Vallone R., Mancini M., Cavinato G.P., Milli S., Costa J.F.C.L.:
 502 Geotechnical characterization of the upper Pleistocene-Holocene alluvial deposits of Roma (Italy) by means of multivariate
 503 geostatistics: crossvalidation results, *Eng. Geol.*, 101, 251–268, DOI: <https://doi.org/10.1016/j.enggeo.2008.06.007>, 2008.

504 Regione Lazio. Viewed May 2021. <https://sciamlab.com/opendatahub/dataset/r_lazio_carta-tecnica-regionale-1991>, 2021.

505 Regione Marche. Viewed May 2021. <[https://www.regione.marche.it/Regione-Utile/Paesaggio-Territorio-](https://www.regione.marche.it/Regione-Utile/Paesaggio-Territorio-Urbanistica/Cartografia/Repertorio/Cartatecnica numerica110000)
 506 [Urbanistica/Cartografia/Repertorio/Cartatecnica numerica110000](https://www.regione.marche.it/Regione-Utile/Paesaggio-Territorio-Urbanistica/Cartografia/Repertorio/Cartatecnica numerica110000)>, 2021.

507 Régnier, J., Bonilla, L., Bard, P., Bertrand, E., Hollender, F., Kawase, H., Sicilia, D., Arduino, P., Amorosi, A., Asimaki, D.,
 508 Boldini, D., Chen, L., Chiaradonna, A., DeMartin, F., Elgamal, A., Falcone, G., Foerster, E., Foti, S., Garini, E.,
 509 Gazetas, G., Gélis, C., Ghofrani, A., Giannakou, A., Gingery, J. R., Glinsky, N., Harmon, J., Hashash, Y., Iai, S., Jeremić, B.,
 510 Kramer, S., Kontoe, S., Kristek, J., Lanzo, G., Lernia, A. di, Lopez-Caballero, F., Marot, M., McAllister, G., Diego Mercerat,
 511 E., Moczo, P., Montoya-Noguera, S., Musgrove, M., Nieto-Ferro, A., Pagliaroli, A., Pisanò, F., Richterova, A., Sajana, S.,
 512 Santisi d'Avila, M. P., Shi, J., Silvestri, F., Taiebat, M., Tropeano, G., Verrucci, L. and Watanabe, K.: International Benchmark
 513 on Numerical Simulations for 1D, Nonlinear Site Response (PRENOLIN): Verification Phase Based on Canonical Cases, *Bull.*
 514 *Seismol. Soc. Am.*, 106(5), 2112–2135, doi:10.1785/0120150284, 2016.

515 Régnier, J., Bonilla, L., Bard, P., Bertrand, E., Hollender, F., Kawase, H., Sicilia, D., Arduino, P., Amorosi, A., Asimaki, D.,
 516 Boldini, D., Chen, L., Chiaradonna, A., DeMartin, F., Elgamal, A., Falcone, G., Foerster, E., Foti, S., Garini, E., Gazetas, G.,
 517 Gélis, C., Ghofrani, A., Giannakou, A., Gingery, J., Glinsky, N., Harmon, J., Hashash, Y., Iai, S., Kramer, S., Kontoe, S.,
 518 Kristek, J., Lanzo, G., Lernia, A. di, Lopez-Caballero, F., Marot, M., McAllister, G., Diego Mercerat, E., Moczo, P., Montoya-
 519 Noguera, S., Musgrove, M., Nieto-Ferro, A., Pagliaroli, A., Passeri, F., Richterova, A., Sajana, S., Santisi d'Avila, M. P., Shi,
 520 J., Silvestri, F., Taiebat, M., Tropeano, G., Vandeputte, D. and Verrucci, L.: PRENOLIN: International Benchmark on 1D
 521 Nonlinear Site-Response Analysis—Validation Phase Exercise, *Bull. Seismol. Soc. Am.*, 108(2), 876–900,
 522 doi:10.1785/0120170210, 2018.

523 Salvatore, E., Spacagna, R. L., Andò, E. and Ochmanski, M. “Geostatistical analysis of strain localization in triaxial tests on
 524 sand”. *Géotechnique Letters* Volume 9 Issue 4, December, pp. 334-339 <https://doi.org/10.1680/jgele.18.00228>, 2019.

525 Schiappapietra, E. and Douglas, J.: Modelling the spatial correlation of earthquake ground motion: Insights from the literature,
 526 data from the 2016–2017 Central Italy earthquake sequence and ground-motion simulations, *Earth-Science Rev.*,
 527 doi:10.1016/j.earscirev.2020.103139, 2020.

528 Schiappapietra, E. and Smerzini, C.: Spatial correlation of broadband earthquake ground motion in Norcia (Central Italy) from
 529 physics-based simulations, *Bull. Earthq. Eng.*, doi:10.1007/s10518-021-01160-7, 2021.

530 **ShakeMap. Viewed May 2021. < <http://shakemap.rm.ingv.it/shake4/>>, 2021.**

531 SM Working Group: Guidelines for Seismic Microzonation, Conference of Regions and Autonomous Provinces of Italy –
 532 Civil Protection Department, Rome. 3 Vol. and DVD. [https://www.centromicrozonazioneismica.it/it/download/category/9-](https://www.centromicrozonazioneismica.it/it/download/category/9-guidelines-for-seismic-microzonation)
 533 [guidelines-for-seismic-microzonation](https://www.centromicrozonazioneismica.it/it/download/category/9-guidelines-for-seismic-microzonation), 2008.

534 Spacagna, R.L. and Modoni, G.: “GIS-based study of land subsidence in the city of Bologna” *Mechatronics for Cultural*
 535 *Heritage and Civil Engineering*, pp.235-256. DOI: 10.1007/978-3-319-68646-2_10, 2018.

536 Tamhidi, A., Kuehn, N., Ghahari, S. F., Rodgers, A. J., Kohler, M.D., Taciroglu, E., Bozorgnia, Y.: Conditioned Simulation
537 of Ground-Motion Time Series at Uninstrumented Sites Using Gaussian Process Regression, *Bulletin of Seismological Society*
538 of America, <https://doi.org/10.1785/0120210054>, 2021.

539 TCSM: Technical Commission for Seismic Microzonation. Graphic and Data Archiving Standards. Version 4.1. National
540 Department of Civil Protection. Rome, [https://www.centromicrozonazioneismica.it/it/download/send/26-standardms-41/71-](https://www.centromicrozonazioneismica.it/it/download/send/26-standardms-41/71-standardms-4-1)
541 standardms-4-1, 2018.

542 Wald, D. J., Worden, C. B., Thompson, E. M. and Hearne, M.: ShakeMap operations, policies, and procedures, *Earthq. Spectra*,
543 doi:10.1177/87552930211030298, 2021.

544 Zhou, H., Li, J. and Chen, X.: Establishment of a seismic topographic effect prediction model in the Lushan Ms 7.0 earthquake
545 area, *Geophys. J. Int.*, 221(1), 273–288, doi:10.1093/gji/ggaa003, 2020.

546

547

548 **Appendix. Spatial correlation structure of the predicted maps**

549 In this appendix we want to preliminarily deal with the spatial correlation of the IM parameters. In fact, the spatial correlation
550 of ground-motion IMs represents a key issue in the seismic risk assessment, particularly in loss analysis (Infantino et al., 2021;
551 Schiappapietra et al., 2020, 2021). The geostatistical tool widely adopted to analyse the spatial correlation of geological and
552 geotechnical data (Paolella et al., 2021, Raspa et al., 2008, Salvatore et al., 2019, Spacagna et al., 2018) is the semi-variogram
553 (Chilès and Delfiner, 2012). The spatial structure is evaluated by assessing the dissimilarity of the variables measured at
554 different locations. First, referring to the variable of interest (in this case, one of the selected IMs), the experimental semi-
555 variogram $\hat{\gamma}(\mathbf{h})$ is calculated from data using the method of moments (Chilès and Delfiner, 2012):

556

$$557 \quad \hat{\gamma}(\mathbf{h}) = \frac{1}{2n(\mathbf{h})} \sum_{i=1}^{n(\mathbf{h})} \{z(\mathbf{x}_i) - z(\mathbf{x}_i + \mathbf{h})\}^2 \quad (\text{A1})$$

558

559 where $z(\mathbf{x}_i)$ and $z(\mathbf{x}_i + \mathbf{h})$ are the observed values of the variable z (i.e., one of the selected IMs) at the location \mathbf{x}_i and $\mathbf{x}_i + \mathbf{h}$
560 separated by \mathbf{h} , and $n(\mathbf{h})$ is the number of pairs at lag \mathbf{h} . Under the assumption of second-order stationary, the semi-variogram
561 increases with \mathbf{h} up to a constant value of $\hat{\gamma}(\mathbf{h})$. In this study, to assess the spatial structure of the variables (predicted IMs),
562 the experimental variogram estimated from the predicted maps is fitted with the best fit model (i.e., the exponential model):

563

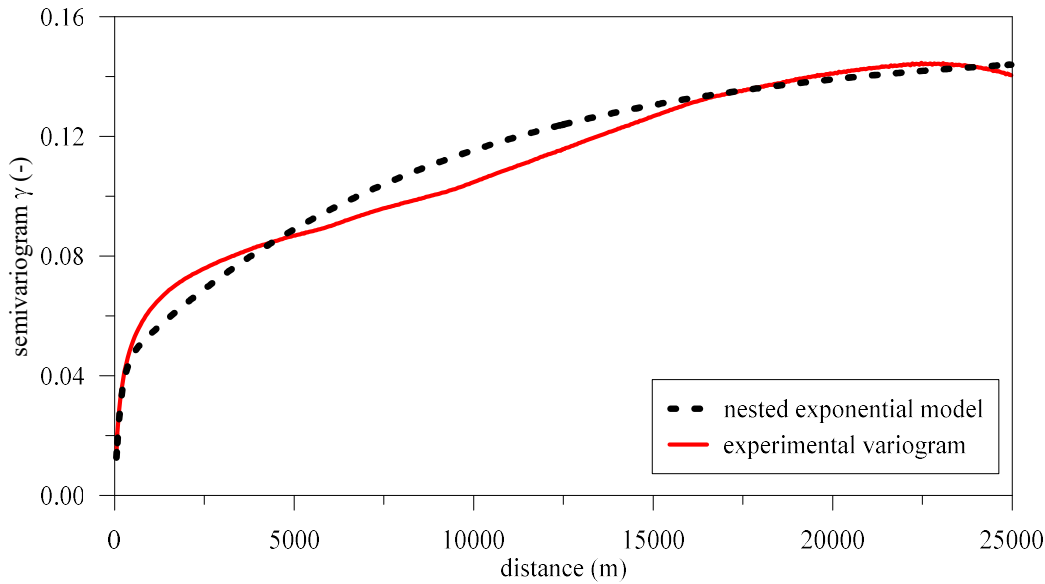
564
$$\gamma(h) = C \left[1 - \exp\left(\frac{-3h}{a}\right) \right] \quad (A2)$$

565

566 where the parameters a and C are called respectively range and sill. The range defines the correlation distance, namely, the
567 separation distance at which the data are spatially independent, and the sill represents the variance of the random process, limit
568 value of $\gamma(h)$.

569 For the Central Italy event occurred on October 30, 2016 and for all the predicted IMs maps (i.e., PGA, $Sa_{0.3}$, Sa_1 ; see Fig. 6
570 and supplementary materials), the spatial structure was performed with the GSTAT package (Pebesma, 2004) of the R software
571 (R Core Team, 2021). The IMs values were extracted from the predicted maps with a regular punctual grid of 50 m x 50 m.
572 The isotropic experimental semi-variograms were computed and fitted with the above-mentioned exponential model. As an
573 example, Fig. A1 shows the semi-variogram of the predicted $Sa_{0.3}$ map. The spatial structure of all predicted IMs maps was
574 characterized by the nested exponential model. The nested variograms highlight the presence of a double structure at different
575 scales, i.e., a short-scale and a long-scale variability.

576



577

578 **Figure A1. Semi-variogram of the predicted $Sa_{0.3}$ map (Central Italy event occurred on October 30, 2016): experimental**
579 **variogram based on the adopted ML approach and best-fitting model (nested exponential).**

580 In this case, two ranges and two sills are obtained for two levels of variability. Table A1 shows the sill and range values for
581 the nested exponential models of all predicted IM maps. The first range, or short-scale structure, captures the first source of
582 variability (first sill) over hundreds of meters induced by lithostratigraphic site conditions and morphological variability. The
583 long-scale structure captures the variability over thousands of meters and could be referred to regional geological units and

584 large-scale morphological features. Furthermore, a significant part of the variance, around 30-40% of the total, are captured at
585 short-scale.

586 An exhaustive treatment of this topic is beyond the scope of this work. We are now studying the spatial variability of input
587 parameters that contribute to generate the target IM maps, and this will be the subject of a future paper. By the way, the
588 preliminary results enlighten the importance to generate ground motion prediction maps with a spatial resolution in the order
589 of hundreds of meters, to improve their quality in terms of predictivity. Seismic hazard maps should also include these
590 specifications to consider the short-scale effects, even if starting from basic hazard maps with a resolution in the order of 2-5
591 km.

592 **Table A1. Sill and range values of the nested exponential model for all the predicted IM maps.**

IM	Short-scale structure		Large-scale structure	
	sill	range [m]	sill	range [m]
PGA	0.01080	600	0.022550	28500
Sa _{0.3}	0.04250	450	0.108000	26700
Sa ₁	0.00530	450	0.010500	21600
Sa ₃	0.00022	750	0.000265	20400

593